Article

Effect of Magnetic Field on the Corrosion of API-5L-X65 Steel Using Electrochemical Methods in a Flow Loop

Shahid Parapurath [1], Arjun Ravikumar [1], Nader Vahdati [1,*] and Oleg Shiryayev [2]

1   Department of Mechanical Engineering, Khalifa University of Science and Technology, SAN Campus, Abu Dhabi P.O. Box 127788, United Arab Emirates; shahidmp2003@gmail.com (S.P.); arjunravikumarch@gmail.com (A.R.)
2   Department of Mechanical Engineering, University of Alaska, Anchorage, 3211 Providence Dr., ECB 301, Anchorage, AK 99508, USA; oshiryayev@alaska.edu
*   Correspondence: nader.vahdati@ku.ac.ae

Abstract: Limited studies have been conducted on the effect of a magnetic field on the corrosion behavior of steels. Investigating the effect on pipeline material in the oil and gas industries will be beneficial regarding corrosion prediction and control. In this work, the effect of a magnetic field on the corrosion process of API 5L X65 carbon steel was investigated in a well-developed flow loop using potentiodynamic polarization curves and electrochemical impedance spectroscopy (EIS). Using permanent magnets and a well-designed corrosion electrode set-up, the corrosion mechanism of API 5L X65 steel was studied at different magnetic orientations and different flow conditions in a NaCl solution. The surface morphology of the corroded samples was studied using a scanning electron microscope, and the micro-morphologies of the corrosion deposits and the surface elemental composition were analyzed. The results show that the presence of a magnetic field increases the corrosion rate of API 5L X65 carbon steel, and that flow velocities and magnetic orientation have a significant influence on the anodic corrosion current. The results of the polarization curves indicate a negative shift in the Tafel curve, leading to an increase in the corrosion rate with the introduction of a magnetic field in the flow system. The results of the EIS show that the charge transfer rate is decreased when a magnetic field is applied. This work provides important direction in terms of the understanding of the combined effect of magnetism and flow on the corrosion in pipelines used in the oil and gas industries.

Keywords: magnetism; pipeline corrosion; carbon steel; flow loop; EIS; LPR

1. Introduction

Pipelines that transport water, oil, gas, chemicals, petroleum products, and other substances are of key importance as they play a crucial role in developing a country's economy. These pipelines are exposed to adverse environments, such as acidic (low pH), high salt concentration, H_2S, and CO_2 environments, where their integrity is critically threatened, resulting in catastrophic incidents. Biezma et al. reported that most of the pipeline failures are due to the effects of corrosion or material failure [1]. Corrosion defects in pipelines are mostly localized, such as pitting corrosion and stress corrosion, rather than uniform corrosion [2,3]. Corrosion in general occurs due to the electron transfer between the metal and aqueous media. This corrosion is enhanced in pipelines due to the presence of flow [4,5]. The presence of different flow helps in the efficient mixing of the different elements in the solution, which prevents the formation of the protective oxide layer on the surface of the material, which, in turn, accelerates corrosion [5]. Several researchers have already investigated the dependence between corrosion and fluid flow [6–8]. Zhang et al., and JanGuo Liu investigated the effect of the velocity of fluid on the elbows of a pipeline and observed that the corrosion rate increased as the velocity increased. They also observed that the corrosion rate increased mostly at a higher velocity [9,10]. Zhang et al., observed

that, at lower fluid velocities, higher pitting corrosion persisted as the protective film was not completely destroyed, whereas, at higher fluid velocities, the protective layer was damaged faster due to the shear at the metal surface [11]. Ajmal et al. and Xu et al., studied the effect of fluid velocity on API X70 and 3003 Al alloys, and they observed that, irrespective of the material, the fluid hydrodynamics had a direct impact on the corrosion rate [12,13].

Even though there are alloyed corrosive resistant materials available, due to cost, mild carbon steel is still commonly used in different industries as a common pipe material [14]. However, low and mild carbon steel materials are highly prone to different types of corrosion. The rate of corrosion is affected by external factors, such as the environment, soil chemistry, water chemistry for submerged pipelines, moisture for buried pipelines, and internal factors, such as the temperature, pressure of the fluid in the pipeline, oxygen concentration of the fluid, dissimilar metal joints, and pH [3]. Considering these factors, it is important to prioritize the routing and location for pipelines in order to achieve longer life with less damage [15].

Studies have also shown that high voltage power lines above pipelines induce a magnetic field in pipeline material [16–18]. Gouda et al. conducted a case study to investigate the effect of an electromagnetic field induced by the overhead transmission power lines. The case study was conducted over a Fayum metallic gas pipeline where three power lines were crossing or parallel to the pipeline. They observed that the current densities change with respect to the length of the pipeline, which, in turn, increases the corrosion rate [19]. A similar study was conducted by Ouadah et al., where they studied the effect of the electromagnetic induction by high voltage power lines on X70 pipelines. In their study, they observed that the effect of the induced magnetic field reduced as the distance between the power line and pipeline increased. They also observed that the increase in the AC current density causes a positive shift in the corrosion potential, which increases the corrosion rate of the material [20].

Researchers have investigated the effect of a magnetic field on the corrosion process of metals where they all observed the effect of magnetohydrodynamic (MHD) theory [21–25]. When a magnetic field is applied to a metal, it influences the process of electrode kinetics, mass transfer, and the formation of a hydroxide/oxide layer by different external forces, such as Lorentz force, paramagnetic gradient force, and gradient magnetic force [26–30]. However, contradictory observations have been made by researchers for different metals under different conditions. Xijiao Li et al., studied the effect of a magnetic field on the dissolution of SS304 and observed that, in an $FeCl_3$ system, the corrosion rate increased under a permanent magnetic field [31]. However, for Alma et al., the results were contradictory as they observed that, for AISI 303 stainless steel in an $FeCl_3$ solution, the corrosion rate decreased along with the number of pits [32]. For the case of copper and titanium alloys in a NaCl solution, the corrosion rate was accelerated, but, for copper and zinc alloys in a HNO_3 solution, the corrosion rate was decreased [21,33]. Xin Zhang et al. studied the effect of a magnetic field on the corrosion performance of different Al-Mg alloys and observed that the Al-Mg alloy with Fe showed a higher corrosion rate and more pits compared to alloys of only aluminum and magnesium, which showed inhibition characteristics under the magnetic field [34]. Hence, it is important to contemplate in detail how a magnetic field can impact pipeline corrosion as there is relatively very little research in this area.

In our study, to address the effect of magnetism on the corrosion of steel pipelines, a flow loop was designed and built. The corrosion rates were evaluated using electrochemical methods and a three-electrode corrosion setup in the flow loop. Our previous study investigated the corrosion rate and its relationship with the temperature, NaCl concentration, flow velocity, and pH in carbon steel [35]. A magnetic-based fiber optic sensor [36,37] was also developed to detect the internal corrosion of pipelines using magnetism and the optical strain sensing technology. The work investigated the effects of magnet size, the magnetic permeability of the pipe material, and the magnetic flux density of the magnet. In the later work [38], a new internal corrosion detection sensor based on the magnetic

interaction between a rare-earth permanent magnet and the ferromagnetic nature of steel was developed with a suitable design that can be easily installed on pipelines and storage tanks. Hence, the aim of this research is to study the impact of a DC magnetic field on a steel specimen in a flow loop system. It examines a specific correlation between the applied permanent magnetic field at different orientations to various flow velocities produced in the flow loop system. This would yield a greater understanding of hydrodynamics and the magnetohydrodynamic effects, which are insufficiently researched but are of great importance considering real-life scenarios. A flow loop was designed for conducting the electrochemical testing under a permanent magnetic field, which is explained in the following sections.

2. Experimental

2.1. Materials and Solution

To study the corrosion behavior of oil and gas pipelines under magnetic field, API 5L X65 carbon steel material with composition as given in Table 1 was used. The samples were designed and machined to obtain a surface area of 1 cm^2 with a diameter of 5 mm and 10 mm height, as shown in Figure 1. Each sample was polished sequentially with 400, 800, 1000, and 1500 silicon carbide emery papers followed by cleansing with ethanol and distilled water and finally air dried. The samples were welded to a copper wire in order to establish electrical connectivity for electrochemical measurement. Two rare earth neodymium N52 magnets of 50 mm diameter and 25 mm height from CMS magnetics with part number ND05080-52NM were used in order to introduce magnetic field in the specimen.

Table 1. Chemical Composition of API 5L X65 (wt. %).

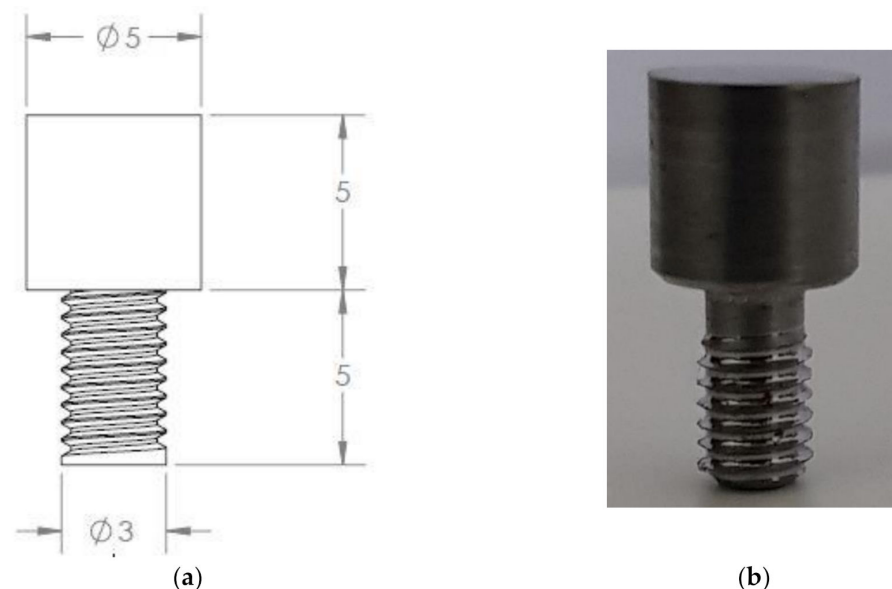| C	Mn	Si	P	S	Cr	Ni	Mo	Cu	V	Ti	Nb	B
0.11	1.06	0.21	0.012	0.0017	0.06	0.09	0.02	0.23	0.004	0.016	0.002	0.0002

Figure 1. API 5L X65 specimen for corrosion testing (**a**) CAD Model, (**b**) actual sample.

Standard 3.5% by weight salt (NaCl) solution was prepared using analytical grade reagents and deionized water for corrosion test. The temperature of the test solution was maintained at room temperature, 22 ± 2 °C. The pH of the test solution was maintained at 6.95 pH, which was ensured using the HI 2550 pH meter. It was decided to run the experiments at room temperature (22 ± 2 °C) and neutral pH (6.95 pH) because these

conditions are easy to achieve and maintain in our lab settings. It is well known that lower pH values generally result in higher corrosion rates. Moreover, higher temperatures result in higher reaction rates and generally speed up corrosion processes. Keeping these two factors relatively constant during the experiment allowed us to keep the focus of our study on the effects of magnetic field and flow velocity.

In real pipelines, particularly oil and gas pipelines, multiphase flow is often encountered. An investigation with multiphase flow would have added many more factors that would have complicated our study, such as how many phases to be used or how many different liquids, solids, and gases to include. To limit the number of variables in our study and place the focus on the effect of magnetic field on corrosion rate, a single-phase flow was only considered. Investigation of the effects of pH and temperature and multiphase flow in conjunction with magnetic fields can be done in the future.

2.2. Experimental Setup

A circulating flow loop system, as shown in Figure 2, was constructed for corrosion testing. It consists of a centrifugal pump, a reservoir, a flow meter, and the test apparatus. The flow loop was constructed with 1 inch PVC pipe. The test solution was supplied from a 70 L reservoir and circulated with the help of a pump. The required flow velocity was maintained at 1 m/s and 2 m/s with the help of a flow control valve and flow meter sensor.

A 3-electrode test apparatus, as shown in Figure 3, was designed, constructed, and placed at a distance of 6.25 m from the end, as shown in Figure 2b, to conduct the corrosion testing in the below flow loop. The test apparatus was placed at a position where the testing was conducted at a fully developed flow condition. The electrodes were placed in such a way that working electrode (WE) and reference electrode (RE) were closely arranged in order to maintain the least resistivity within the electrolyte. The magnets were fixed on the apparatus, as shown in Figure 3c, where the flux intensity of magnetic field was measured at the surface of the specimen as 1500 gauss. The orientation of the magnets was varied for zero flow (A), 1 m/s (B), and 2 m/s (C) as no magnet (1), N-S (2), and N-N (3).
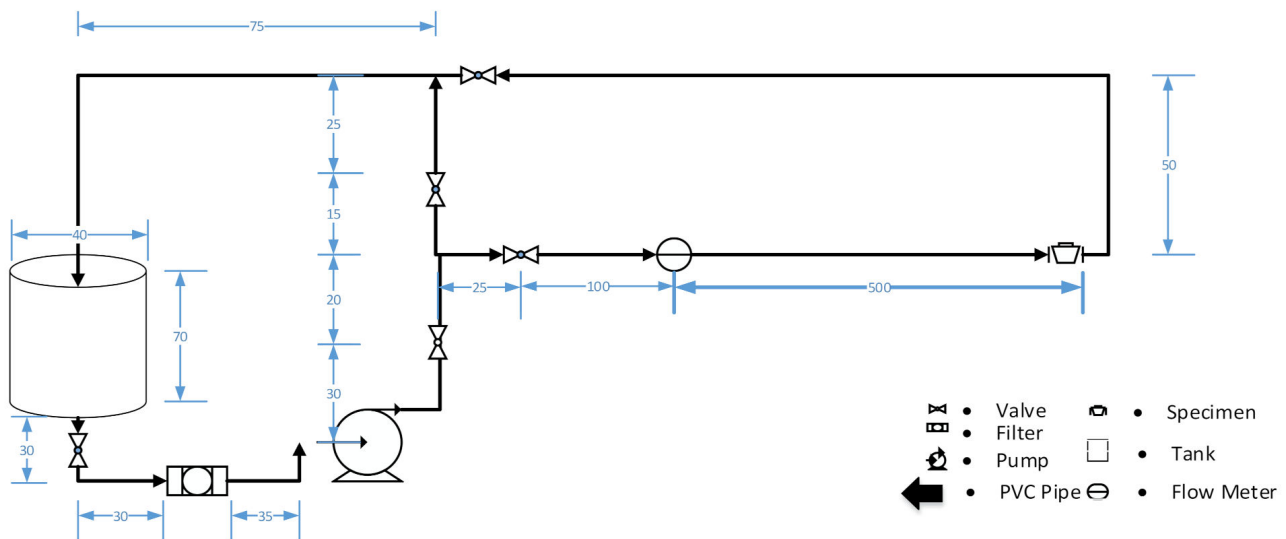
All dimensions are in centimeters

(**a**)

Figure 2. *Cont.*

Figure 2. (a) Schematic diagram of the flow Loop, (b) flow direction and specimen location, (c) actual installed flow loop.

2.3. Electrochemical Measurements

The test apparatus shown in Figure 3b consists of a 3-electrode setup, where WE is the steel sample under test with 1 cm^2 exposed area, graphite electrode as CE, and Ag/AgCl electrode as RE. For each case, an open circuit potential (OCP) was applied for 1 h to make the system stable. Linear polarization rate (LPR), potentiodynamic polarization, and electrochemical impedance spectroscopy (EIS) were conducted for each case with the help of Gamry Ref 600 Potentiostat. LPR measurements were conducted at a potential range of ±20 mV at a scan rate of 0.1 mV/s. Potentiodynamic polarization measurements were performed by sweeping voltage from −1200 mV to 800 mV vs. OCP at a scan rate of 1 mV/s, by which the Tafel constants were determined. The obtained curves were then fitted using Gamry Echem Analyst software, which uses the Stern–Geary equation as given in Equation (1), where R_p is the polarization resistance and I_{corr} is the corrosion current density.

$$R_p = \frac{B}{I_{corr}} \tag{1}$$

B is the constant, which is calculated from Equation (2) where β_a and β_b are the anodic and cathodic constants.

$$B = \frac{\beta_a \, \beta_b}{2.3 \, (\beta_a + \beta_b)} \tag{2}$$

The corrosion rate was then calculated from Equation (3), where K is a constant consistent with the units for corrosion rate, E_w is the equivalent weight, D is the density, and A is the area of the test sample.

$$Corrosion\ Rate = \frac{I_{corr}\ K\ E_w}{D\ A} \tag{3}$$
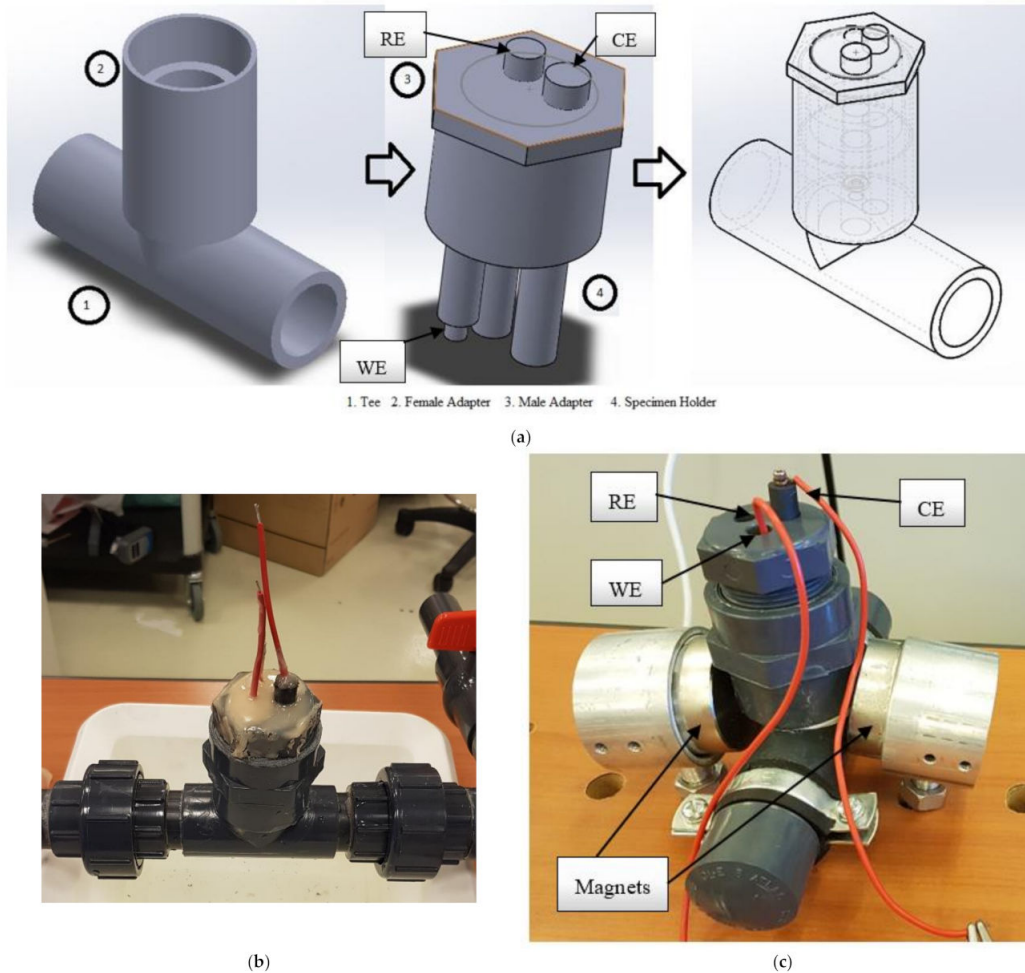
Figure 3. Electrochemical test apparatus (**a**) CAD design (**b**) on flow loop (**c**) with magnets.

In the electrochemical impedance spectroscopy (EIS) method, an alternating current is applied to the electrode system with an amplitude in the range of 5 to 20 mV and the response to the disturbance is measured. EIS works in the frequency domain and the interface is correlations between electrochemical system parameters and characteristic impedance elements, such as the capacitance of the electrode surface and the polarization resistance and the inductance. The most common method to represent and analyze the impedance of the electrode under investigation is using equivalent circuit modelling. The electrochemical processes in the corrosion system can be considered equivalent to an electric circuit that consists of elements such as resistance, capacitors, inductors, etc. For the corrosion system, it is assumed that the electrochemical reactions occur with relatively slow charge transfer, such as the rate determining step to evaluate the impedance. The impedance is expressed in terms of a magnitude, Z. The impedance relates the sinusoidal disturbance potential and the sinusoidal current response. A Nyquist plot, which represents impedance vectors (Z′) real and imaginary part (Z″) at different measured frequencies, are obtained. In this case, the EIS measurements were carried out by applying a sinusoidal voltage excitation of 5 mV in a frequency range of 100 KHz to 10 mHz for 10 points per

decade. The data were then fitted with the help of an equivalent circuit using Gamry Echem Analyst software.

2.4. Surface Analysis

After the corrosion testing, each sample was cleaned with ethanol and distilled water and dried in air. The surface morphology of corroded samples was analyzed by scanning electron microscope (SEM) and Alicona InfiniteFocus. Quanta FEI 250 was used to obtain the micro-morphologies of the corrosion deposit along with their surface elemental composition. Surface roughness and profile roughness were measured using InfiniteFocus (IF-MeasureSuite) software.

3. Results

3.1. Polarization Curves Measurements

The anodic and cathodic polarization curves of the API 5L X65 carbon steel electrode in the NaCl solution in the presence and absence of a magnetic field at various flow concentrations are given in Figure 4. The anodic current increases gradually as the flow velocity increases. However, the presence of a magnetic field in various flow conditions increases the corrosion effect exponentially. From Figure 4a–c, it can be observed that the Tafel curves show a negative shift, indicating that corrosion increases with respect to the effect of a magnetic field. Table 2 presents the fitting parameters of the API 5L X65 carbon steel in various given conditions. Both I_{corr} and E_{corr} increase with the increase in the flow velocity. As for the Tafel constants, they are higher for the anodic polarization curve than for the cathodic polarization curve, indicating that the anodic reaction is more dominant than the cathodic reaction in the half cell reaction process. The polarization resistance values show a decreasing trend, which corresponds with the corrosion rate that increases from A1 to C3. Corrosion rates, shown in Table 2 in the last column, have a maximum standard deviation of $\pm2\%$.

(a)
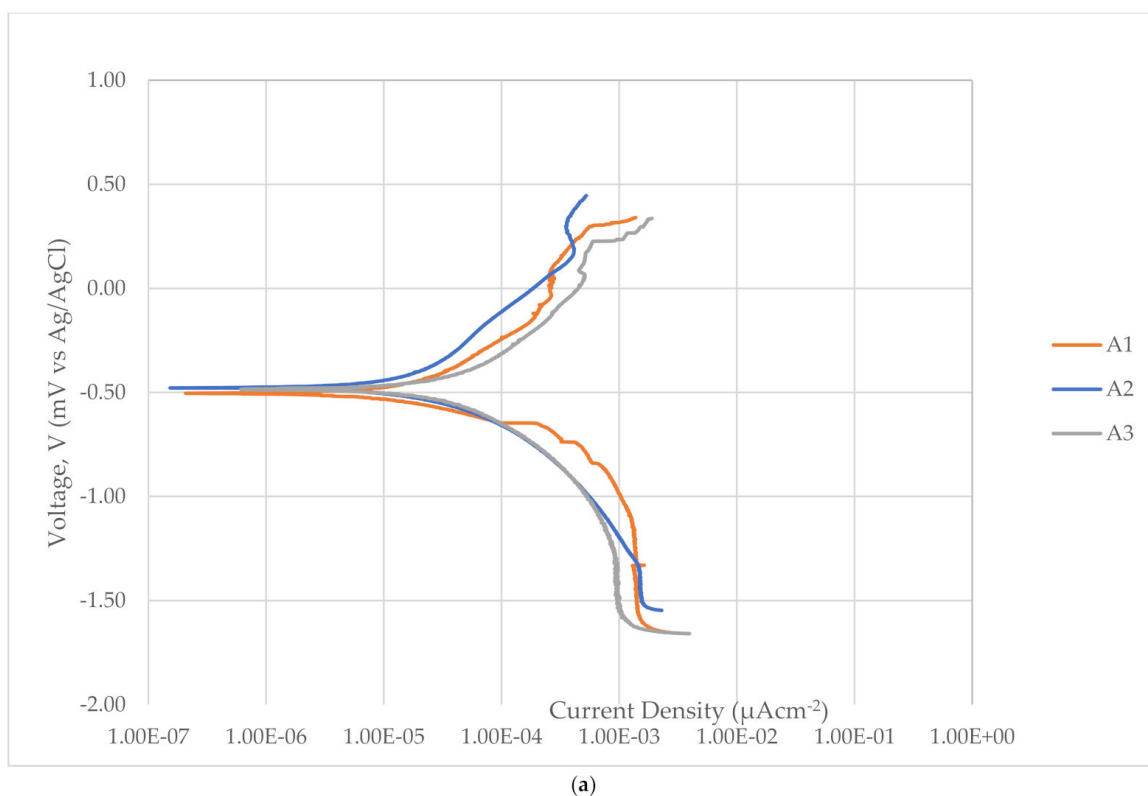
Figure 4. *Cont.*
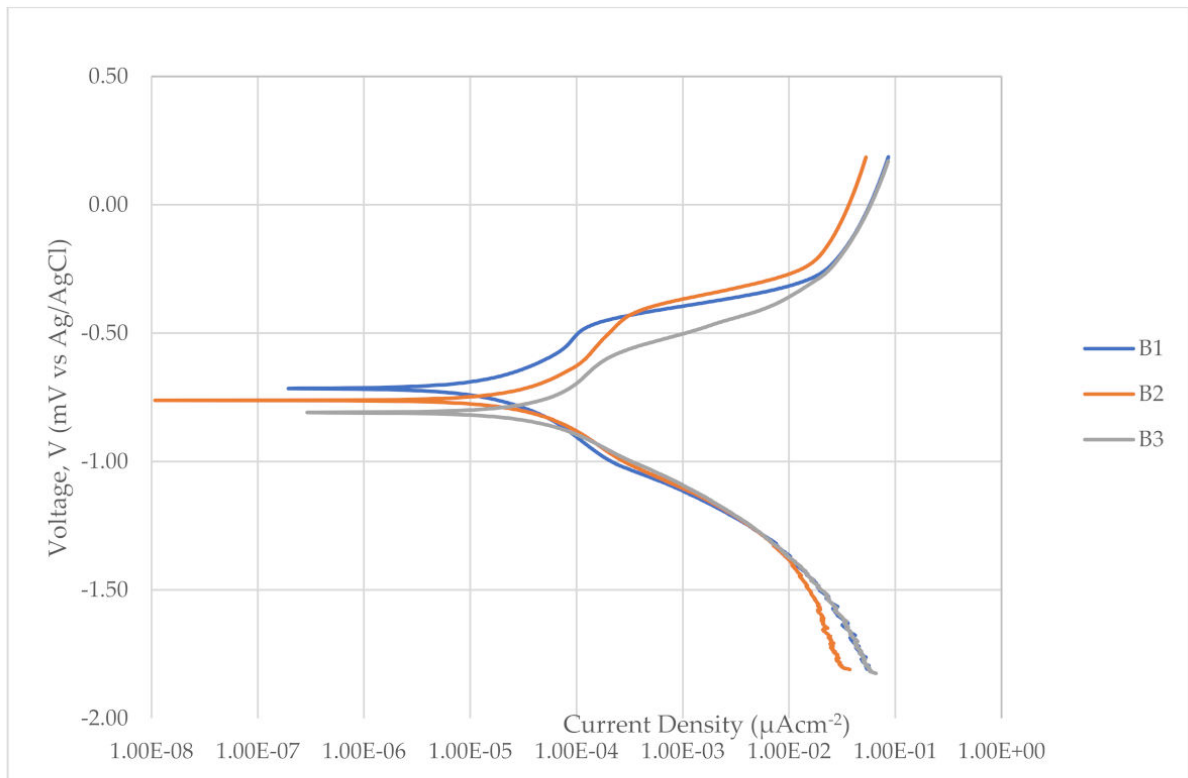
(**b**)
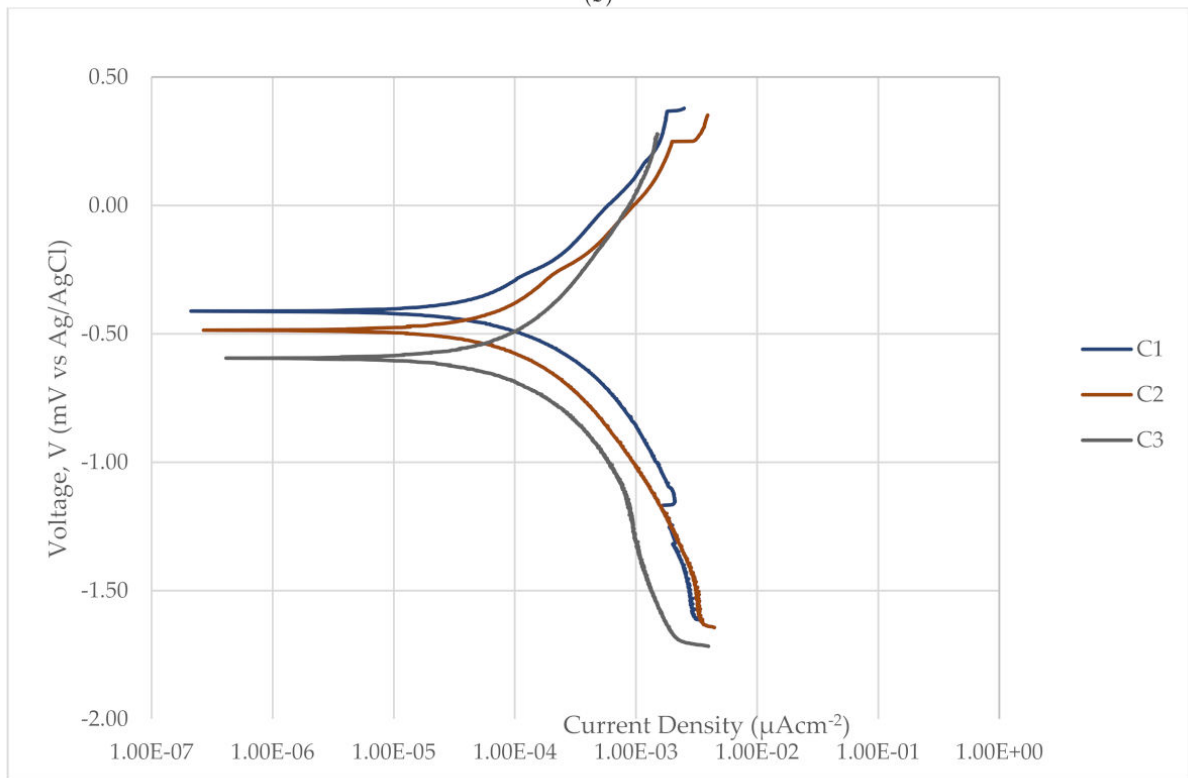
(**c**)

Figure 4. Potentiodynamic polarization curve (**a**) zero Velocity, (**b**) 1 m/s, (**c**) 2 m/s.

Table 2. Polarization Data.

Sample Name	Flow Vel. (m/s)	Magnet Orientation	β_a (V/decade)	$|\beta_c|$ (V/decade)	I_{corr} (μAcm^{-2})	E_{corr} (mV vs. Ag/Agcl)	R_p (Ωcm^2)	Corrosion Rate (mmpy)
A1	0	No Magnet	5.76×10^{-1}	2.13×10^{-1}	19.4	-478	2879	0.28
A2	0	N–S	3.71×10^{-1}	1.94×10^{-1}	21.4	-505	1998	0.33
A3	0	N–N	5.43×10^{-1}	5.04×10^{-1}	62.3	-485	1337	1.00
B1	1	No Magnet	3.04×10^{-1}	2.94×10^{-1}	25.5	-715	1438	0.70
B2	1	N–S	4.79×10^{-1}	3.73×10^{-1}	65.5	-762	906.3	1.11
B3	1	N–N	5.76×10^{-1}	3.27×10^{-1}	90.1	-809	734.6	1.54
C1	2	No Magnet	5.30×10^{-1}	3.73×10^{-1}	97.7	-412	776.8	0.78
C2	2	N–S	6.45×10^{-1}	4.34×10^{-1}	112	-486	690	1.47
C3	2	N–N	7.91×10^{-1}	6.02×10^{-1}	149	-595	702.5	2.39

For A1 at the zero flow, no magnet condition, the CR is observed as 0.28 mmpy (mm/yr), which then increases to 0.33 mmpy at A2 for the N–S magnetic field and 1.00 mmpy at A3 when the N–N magnetic field is applied. The corrosion rate then increases again when both the magnetic field and a velocity of the fluid inside the pipeline is increased. This can be observed from B1 to C3. At B1, the corrosion rate is observed as 0.70 mmpy, which then increases to 1.11 mmpy at B2 and 1.54 mmpy at B3. The maximum CR is observed when the flow velocity is maximal, that is at 2 m/s. At C1, the CR is observed as 0.78, mmpy, which then increases at C2 where the CR is 1.47 mmpy, and at C3 the CR is 2.39 mmpy.

3.2. Electrochemical Impedance Spectroscopy (EIS)

Figure 5 shows the Nyquist plots for the API 5L X65 samples under different flow and magnetic field conditions. Evidently, all the graphs show a regular capacitive loop of a single semicircle due to the double layer interface formed between the metal and solution interface for different conditions. The equivalent circuit, generated using Gamry Echem Analyst software, used to analyze the curves obtained from the Nyquist plot, is given in Figure 6, where R_s is the solution resistance, C_f is the capacitance due to the corrosion product, R_f is the film resistance, R_{ct} is the charge transfer resistance, and a CPE (constant phase element) is used to obtain the double layer capacitance Q. From Figure 5a–c, it is evident that the capacitance arc decreases as the flow velocity is increased and it decreases when the magnetic field is applied. After fitting the equivalent circuit, the obtained EIS kinetics parameters are listed in Table 3.

From Figure 5a, where the velocity is 0 m/s, the R_{ct} value for the no magnetic condition is found as 3310 Ωcm^2, which is highest from A1 to C3. For the same velocity of 0 m/s, when an N–S magnetic field is applied, the value decreases to 2330 Ωcm^2, whereas, for the N–N magnetic field, the R_{ct} values decrease again to 1800 Ωcm^2. This depicts that the charge transfer is higher when a magnetic field is applied to the API 5L X65 samples. As the velocity gets increased to 1 m/s and 2 m/s, the R_{ct} values decrease significantly, showing that flow can cause higher electron transfer in the presence of a magnetic field. By analyzing Figure 5b, it can be observed that, for sample B1, the R_{ct} value decreases to 1420 Ωcm^2, which is almost half of the R_{ct} obtained at A1. A similar result is observed for B2 and B3, where the R_{ct} decreases again to 870.4 Ωcm^2 and 698.5 Ωcm^2. The same kind of reaction kinetics as with B1–B3 is obtained for samples at 2 m/s. For sample C1 at 2 m/s, the R_{ct} value decreases to 723.9 Ωcm^2, whereas, for C2 and C3, the R_{ct} values again decrease to 683.7 Ωcm^2 and 304.2 Ωcm^2. The characterization results depict that there is a significant increase in corrosion as the charge transfer rate is decreased when a magnetic field is applied.
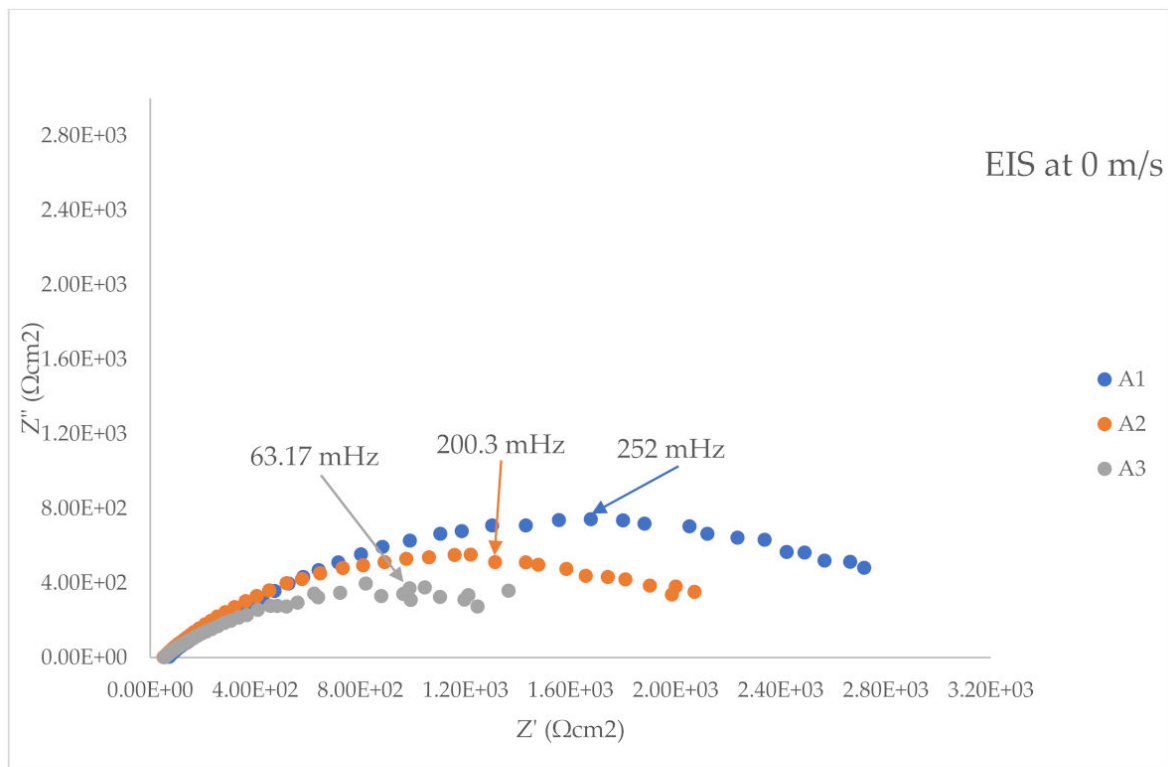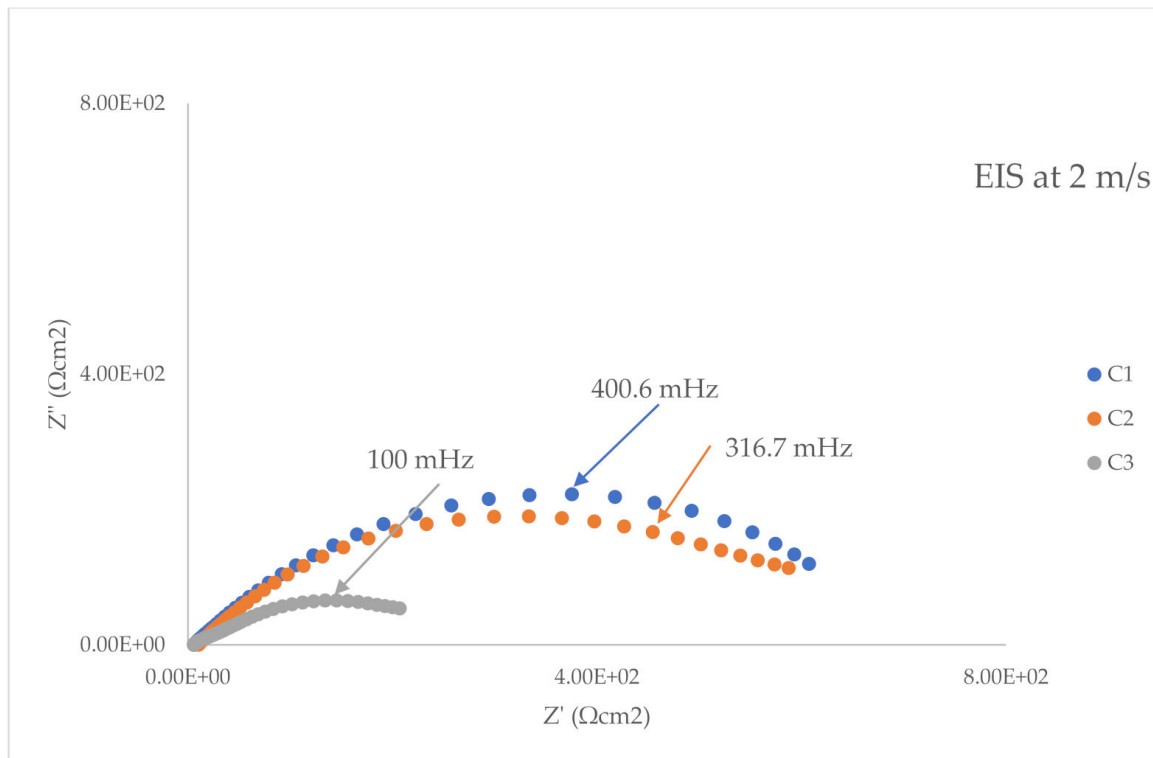
(**a**)
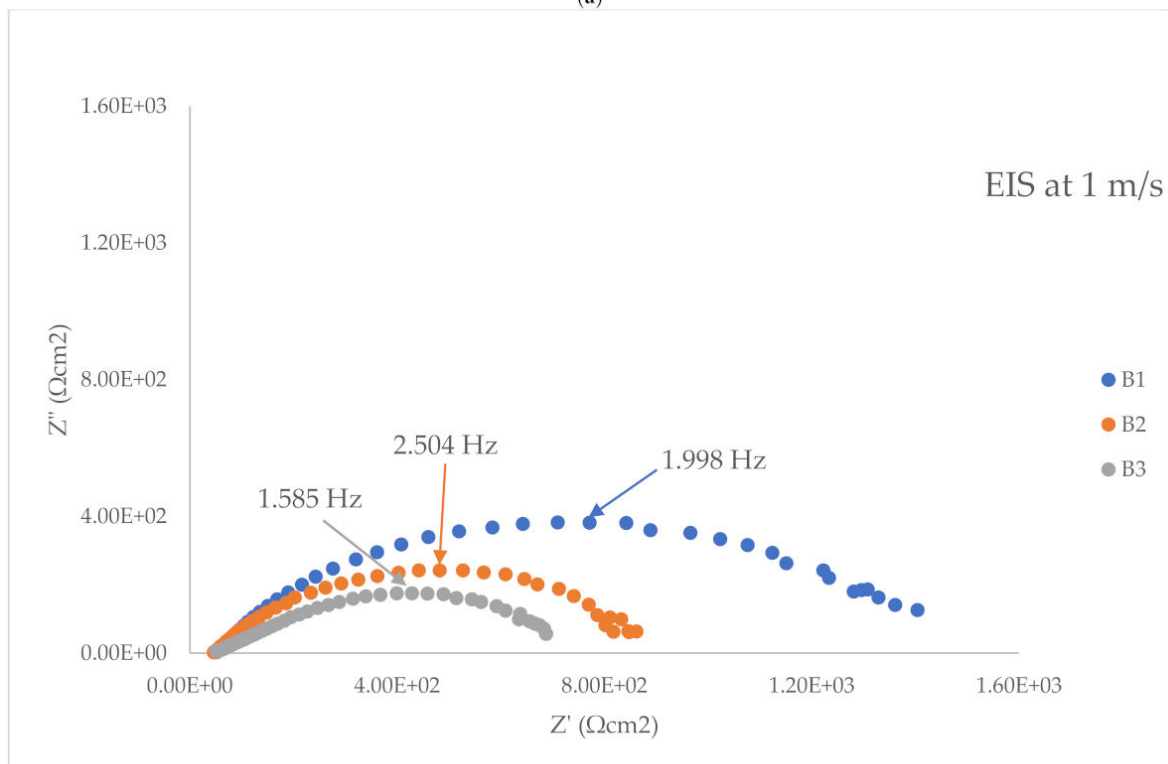
(**b**)

Figure 5. *Cont.*

(**c**)

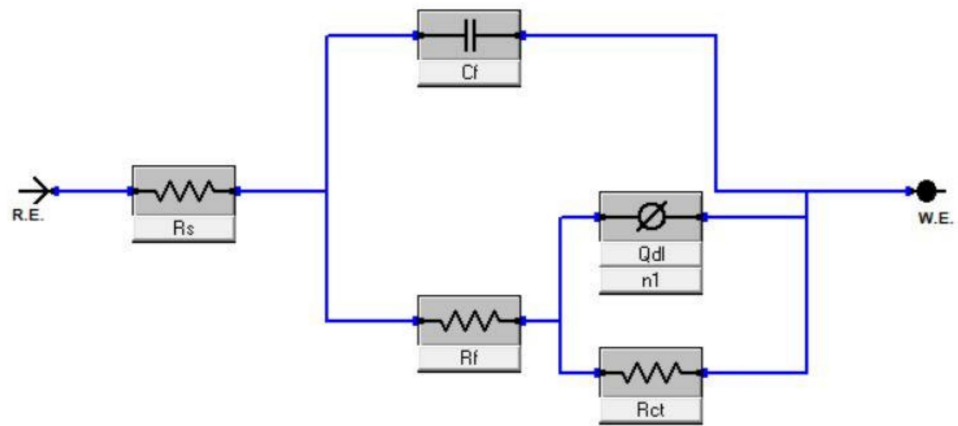**Figure 5.** EIS Nyquist plots (**a**) 0 m/s, (**b**) 1 m/s, (**c**) 2 m/s.

Figure 6. EIS equivalent circuit.

Table 3. Fitting parameters of EIS of API 5L X65.

Sample Name	R_s (Ωcm^2)	Q_{dl} ($s^n \Omega^{-1} cm^{-2}$)	n1	R_{ct} (Ωcm^2)	R_f (Ωcm^2)	C_f ($F cm^{-2}$)
A1	71.2	2.55×10^{-4}	5.29×10^{-1}	3.31×10^{-3}	490.3	3.65×10^{-7}
A2	51.19	3.15×10^{-4}	5.74×10^{-1}	2.33×10^{-3}	373.8	2.67×10^{-6}
A3	54.95	6.79×10^{-4}	4.93×10^{-1}	1.80×10^{-3}	100.3	2.86×10^{-6}
B1	49.62	1.34×10^{-4}	6.40×10^{-1}	1.42×10^{-3}	4.295	1.10×10^{-6}
B2	42.3	1.93×10^{-4}	6.41×10^{-1}	870.4	4.375	1.78×10^{-7}
B3	49.73	3.92×10^{-4}	5.38×10^{-1}	698.5	13.54	5.49×10^{-7}
C1	5.702	7.62×10^{-4}	6.48×10^{-1}	723.9	4.778	2.10×10^{-5}
C2	10.18	5.99×10^{-4}	6.33×10^{-1}	683.7	4.735	1.38×10^{-5}
C3	5.733	5.35×10^{-3}	4.98×10^{-1}	304.2	5.127	6.92×10^{-5}

3.3. Surface Roughness and Profile Roughness

Table 4 illustrates the surface topography of the API 5L X65 samples obtained from the Alicona InfiniteFocus 3D measurement tool. These images were then analyzed with the help of the IF Measure suite provided by Alicona in order to obtain the surface roughness parameters, such as S_a (average aerial roughness), V_{mp} (peak material volume), V_{mc} (core material volume), V_{vv} (core valley volume), and profile roughness parameters, such as R_a (average profile roughness). All the parameters were obtained by following ASME standard B 46.1.

Table 4. Surface roughness at $5\times$ magnification using Alicona InfiniteFocus.
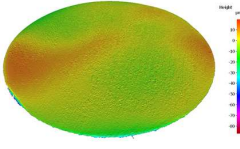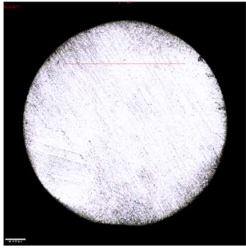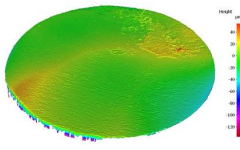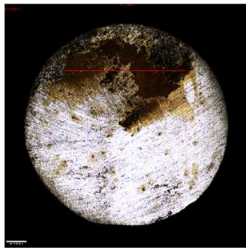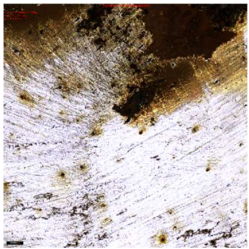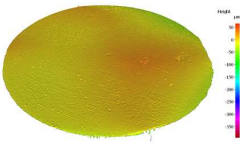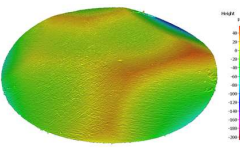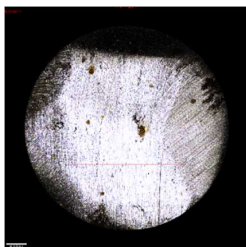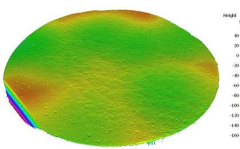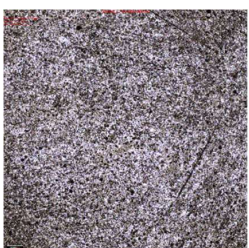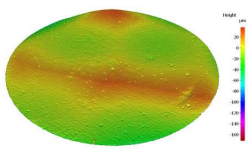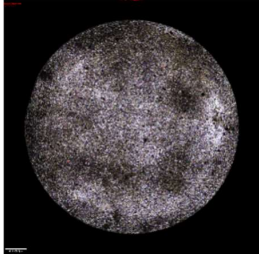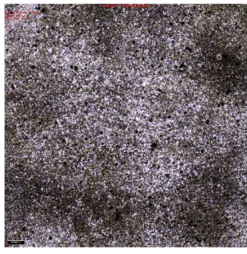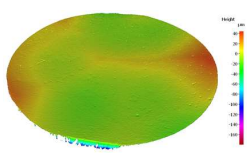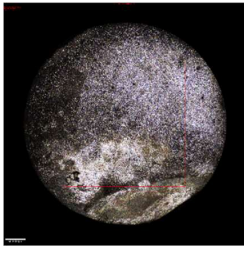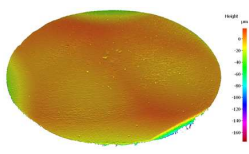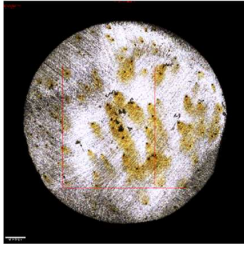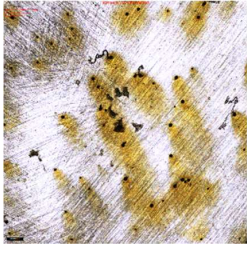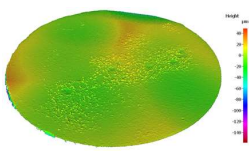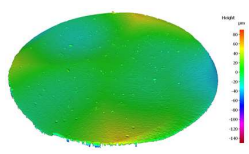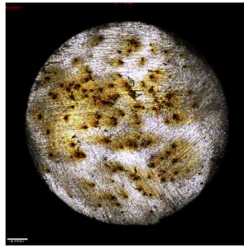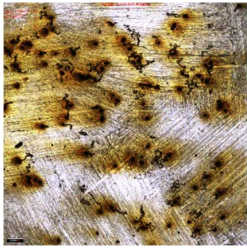
Sample Number	3D View	3D View with Distribution	Top View with Selection (500 µm)	Top View Filtered Area 3 mm $\times$ 3 mm (200 µm)
Before Corrosion				
A1				
A2				
A3				
B1				

Table 4. *Cont.*

Sample Number	3D View	3D View with Distribution	Top View with Selection (500 μm)	Top View Filtered Area 3 mm × 3 mm (200 μm)
B2				
B3				
C1				
C2				
C3				

The surface roughness parameters and profile roughness parameters are given in Table 5. For the samples before corrosion, the S_a is found to be 3.4 μm, which then increases as the corrosion rate increases. For the zero flow condition, when there is no magnetic field, the S_a value increases to 7.4 μm. However, when an N–S magnetic field is applied, at A2, the S_a value obtained is 8.4 μm, and, at A3 when a N–N magnetic field is applied, the S_a value obtained is 8.4 μm. Only a very small increase of 0.06 μm is observed when the polarity is changed. Similar results are observed for samples B1 to B3. For 1 m/s velocity in the no magnetic field condition, an S_a value of 6.5 μm is observed, which then increases to 8.2 μm at B2 and 9.23 at B3. When a flow velocity of 2 m/s is applied, the material loss

from the surface is very uniform as the S_a value obtained is 3.5 μm, which is relatively small compared to other cases. However, it again increases to 7 μm at C2 and 7.7 μm at C3. As the corrosion rate increases from A1 to C3; the S_a values also increase for the same flow velocity alone, but their increase is not relative to nature when a magnetic field is applied. For sample B1, the S_a value is observed as 6.5 μm, but it then reduces to 3.5 μm for C1. This shows that the there is no direct relation between the corrosion and the surface topography in different cases.

Table 5. Roughness Data.

Sample Number	S_a(μm)	V_{mp} (mL/m^2)	V_{mc} (mL/m^2)	V_{vv} (mL/m^2)	R_a(nm)
Before Corrosion	3.3984	0.1914	3.7594	0.3698	131.9685
A1	7.4325	0.5562	8.1134	0.5903	234.0398
A2	8.3968	0.3755	9.1289	0.5769	117.2709
A3	8.4291	0.5501	9.8871	0.408	109.5201
B1	6.4986	0.2549	7.6842	0.5426	108.5177
B2	8.2364	0.4605	9.5185	0.6602	241.608
B3	9.2522	0.5572	10.403	0.4405	245.7435
C1	3.4676	0.3517	3.8541	0.2111	70.1792
C2	7.0254	0.7044	7.4242	0.4545	312.4567
C3	7.7112	1.1774	7.8804	0.7421	63.16683

As for the profile roughness, the R_a value does not show any relation with the corrosion because the profile roughness measurement is done on a very small region, in our case, at 50X magnification, which is given in Table 6. This could be observed from Table 5, where, for the samples before corrosion, the R_a is 132 nm, which then increases to 234 nm for A1 at zero flow and no magnetic field but then decreases to 117 nm for A2 at zero flow and the N–S magnetic field condition, and then again reduces to 109 nm for A3 at zero flow and the N–N magnetic condition. Similar results are observed for the cases when the velocities are 1 m/s and 2 m/s.

Table 6. Profile roughness images at 50× magnification using Alicona InfiniteFocus.
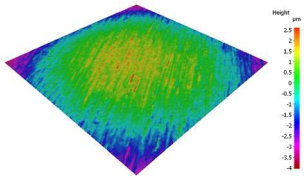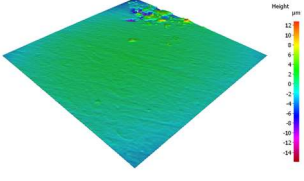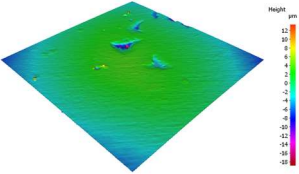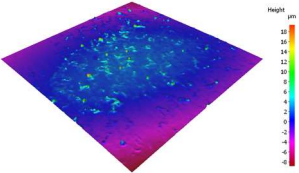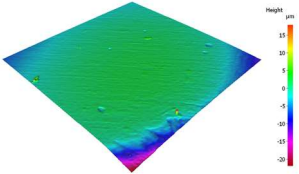
Sample Number	3D View 50×	3D View Distributed 50×	Location 1 (100 μm)
Before Corrosion			
A1			

Table 6. *Cont*.

Sample Number	3D View 50×	3D View Distributed 50×	Location 1 (100 μm)
A2			
A3			
B1			
B2			
B3			

Table 6. *Cont.*

Sample Number	3D View 50×	3D View Distributed 50×	Location 1 (100 μm)
C1			
C2			
C3			

V_{mp} depicts the corrosion product, V_{mc} depicts the core base metal, and V_{vv} depicts the pit formed on the surface of the metal. For the no corrosion condition, the V_{mp} value is about 0.2 mL/m^2, which then increases as the corrosion rate increases. From Table 2, we observed that the highest corrosion rate is for C3, and, from Table 5, we can see that the highest V_{mp} and V_{vv} are for C3, which shows that the corrosion product formation and pit formation is the highest for C3. The same explanation given for S_a follows here as there is no correlation between cases when there is a magnetic field applied.

3.4. SEM

To study the corrosion behavior of the API 5L X65 samples after potentiodynamic polarization, the SEM technique was used to analyze samples A1 to C3. Table 7 shows the SEM images of the sample surfaces along with their EDX data for samples at 0 m/s (A1, A2, A3), 1 m/s (B1, B2, B3), and 2 m/s (C1, C2, C3). The first row of Table 7 gives the SEM image of the API 5L X65 samples before corrosion, completely polished without any corrosion. The EDX data show that the Fe concentration is the highest among all the other cases, depicting the least corrosion on the surface. It is a well-known fact that EDX results only show the elemental composition of the specimen surface and cannot indicate oxide layer formation, but the EDX data clearly show the oxygen elemental concentration increasing and iron elemental concentration decreasing, thus indirectly implying oxide layer formation on the surface of the specimen. The SEM images confirm this observation.

For samples A1, A2, and A3 at 0 m/s flow velocity, the surface has started to become covered with corrosion product, which is formed by the reaction between the Fe, O_2, and OH- forming the ferric oxyhydroxide. This was revealed with the help of EDX data, which show the traces of the Fe concentration reducing and the oxygen concentration increasing along with the presence of chlorine as compared to fresh samples. For samples B1, B2, and B3 at 1 m/s flow velocity, the surface has less formation of loosely covered corrosion product as compared with A1, A2, and A3, which may have been removed by the velocity of the liquid in the system. However, we can observe the formation of small pits on the surface initiating localized corrosion over the metal surface. The EDX data for samples B1 to B3 show the formation of both ferric oxyhydroxide and ferric chloride, which is found in the pits generated at the surface. For samples C1, C2, and C3 at 2 m/s velocity, the material surface shows the formation of both the corrosion product and pits, but larger in size and greater in number as compared to samples at 1 m/s. The EDX data show that the chlorine concentration has increased as compared to samples at 1 m/s, which is because of the formation of more pits on the metal surface.

Table 7. SEM Images of API 5L X65 samples.
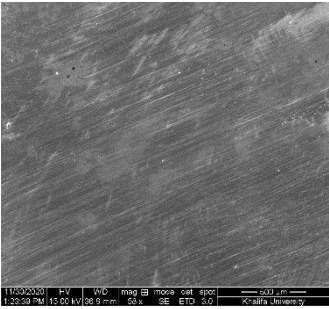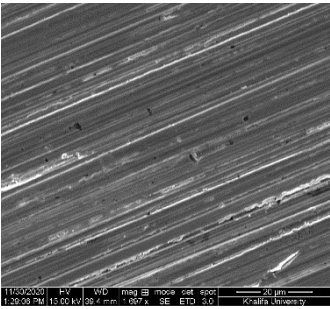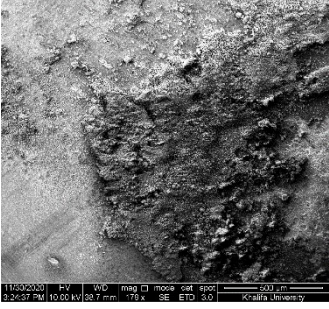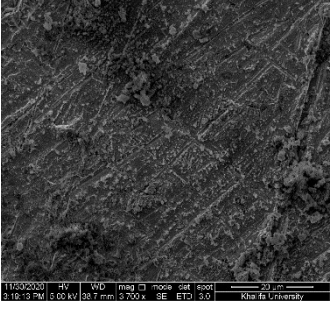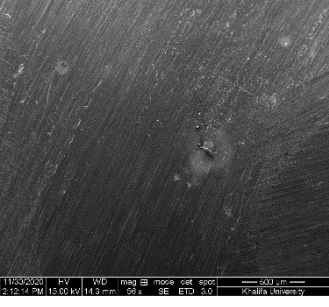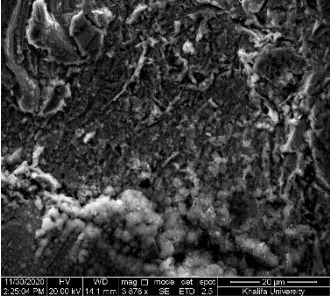
Sample Name	500 µm	20 µm	SEM EDX		
Before Corrosion			Element	Wt %	At %
			C K	1.28	5.48
			O K	1.57	5.05
			MnK	1.86	1.74
			FeK	95.29	87.73
A1			Element	Wt %	At %
			C K	1.24	5.16
			O K	2.52	7.90
			NaK	0.41	0.88
			ClK	0.30	0.42
			MnK	1.51	1.29
			FeK	94.02	84.35
A2			Element	Wt %	At %
			C K	2.61	10.27
			O K	3.07	9.04
			NaK	0.63	1.28
			ClK	0.37	0.50
			MnK	1.56	1.34
			FeK	91.77	77.57

Table 7. *Cont.*
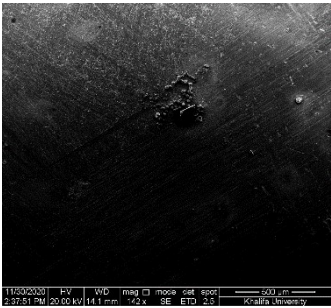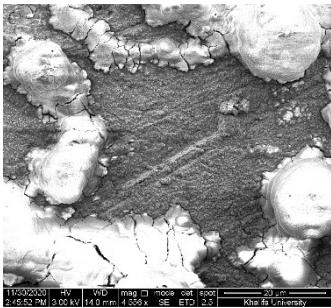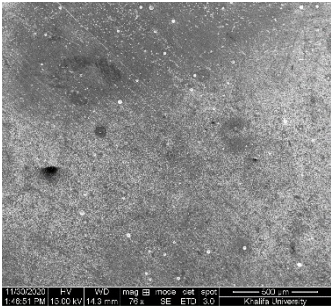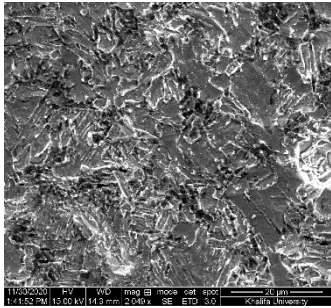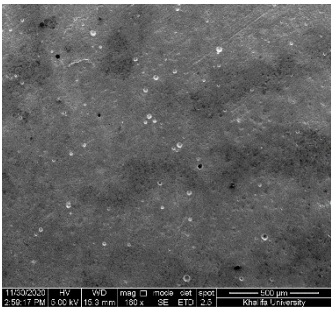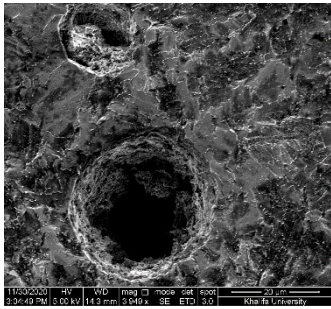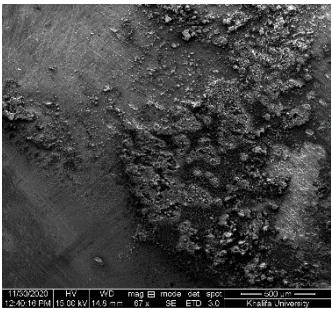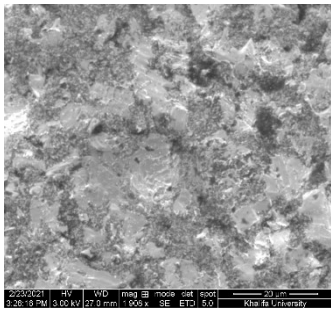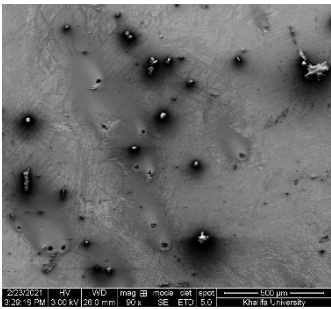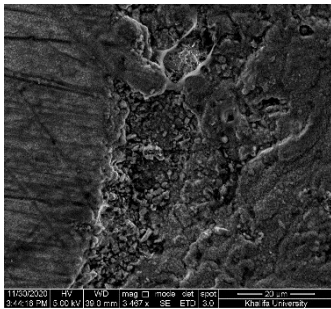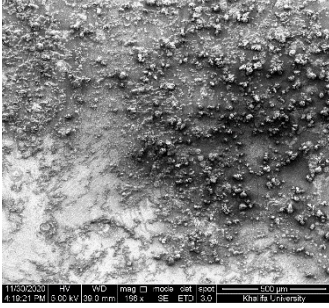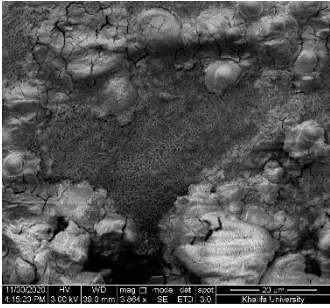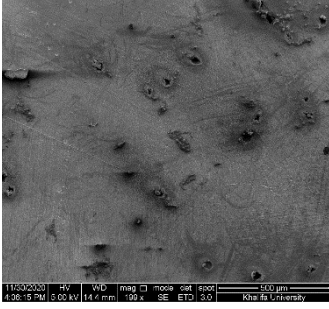
Sample Name	500 μm	20 μm	SEM EDX		
A3			Element	Wt %	At %
			C K	1.69	5.64
			O K	13.20	32.98
			NaK	0.29	0.50
			ClK	0.38	0.43
			MnK	1.42	1.04
			FeK	83.01	59.42
B1			Element	Wt %	At %
			C K	3.73	14.51
			O K	2.10	6.15
			NaK	0.33	0.67
			ClK	0.10	0.13
			MnK	1.61	1.37
			FeK	92.14	77.17
B2			Element	Wt %	At %
			C K	2.95	11.59
			O K	2.73	8.04
			NaK	0.45	0.93
			ClK	0.22	0.29
			MnK	1.99	1.71
			FeK	91.66	77.45
B3			Element	Wt %	At %
			C K	2.90	9.99
			O K	9.54	24.69
			NaK	0.22	0.40
			ClK	0.36	0.42
			MnK	2.27	1.71
			FeK	84.72	62.80
C1			Element	Wt %	At %
			C K	2.21	8.59
			O K	4.33	12.63
			NaK	0.47	0.96
			ClK	0.30	0.40
			MnK	1.81	1.54
			FeK	90.87	75.89

Table 7. *Cont.*

Sample Name	500 μm	20 μm	SEM EDX		
C2			Element	Wt %	At %
			C K	1.60	6.04
			O K	6.38	18.11
			NaK	0.73	1.44
			ClK	0.43	0.55
			MnK	1.83	1.51
			FeK	89.03	72.35
C3			Element	Wt %	At %
			C K	1.81	5.66
			O K	16.41	38.61
			NaK	0.37	0.61
			ClK	0.52	0.55
			MnK	1.62	1.11
			FeK	79.28	53.45

4. Discussion

The potentiodynamic polarization data from Table 2 and the SEM images from Table 7 indicate that the corrosion rate and corrosion product formation vary from A1 to C3 of the API 5 L X65 samples for the various flow and magnetic conditions. These reactions occur due to the presence of various ions, such as H^+, OH^-, Fe^{2+}, and Fe^{3+}, formed in the solution. During the reaction of carbon steel in a near-neutral NaCl solution, the cathodic process may include the reduction of H^+ and OH^- ions, which is shown in Equations (4) and (5), and the anodic reaction includes the dissolution of iron, as shown in Equations (6) and (7).

Cathodic Reaction:

$$O_2 + 2H_2O + 4e^- \rightarrow 4OH^- \tag{4}$$

$$2H^+ + 2e^- \rightarrow H_2 \tag{5}$$

Anodic Reaction:

$$Fe \rightarrow Fe^{2+} + 2e^- \tag{6}$$

$$Fe^{2+} \rightarrow Fe^{3+} + e^- \tag{7}$$

The presence of sodium chloride in the corrosion process complicates the corrosion mechanism depending upon the oxygenated and deoxygenated environment. Chloride ions accelerate the anodic reactions by forming intermediate corrosion species, and, due to the higher activity of H^+, the solution pH is decreased [39]. Fe^{2+} ions then react with the OH^- ions from the cathodic reaction in the presence of chloride ions to form the following corrosion product, as given in Equations (8), (9) and (10).

$$Fe^{2+} + 2OH^- \rightarrow Fe(OH)_2 \tag{8}$$

$$4Fe(OH)_2 + O_+ + 2H_2 \rightarrow 4Fe(OH)_3 \tag{9}$$

$$Fe(OH)_3 \rightarrow FeOOH + H_2O \tag{10}$$

The hydroxyl (OH^-) ions will be present in addition to the dissolved oxygen under high Cl^- concentrations, leading to the formation of FeOOH, ferric oxyhydroxide [40]. On the metal surface, Cl^- competes with the dissolved O_2 or OH^-, and Cl^- favors the

hydration of the metal ions and results in the increase in the metal ion migration from the metal surface to the bulk of the solution [41]. The most common ferric oxyhydroxide corrosion products are α-FeOOH and γ-FeOOH in high salinity in oxygenated systems. For samples B1 to C3, small pits are observed on the surface after the potentiodynamic polarization, which is shown in Table 7. These pits are formed by the reaction of the Cl^- ions with the Fe ions present in the solution, which is shown in Equations (11)–(15) [42–44]. The chloride ions present in the electrolyte solution aggressively attack the steel surface at the anodic region, which leads to the dissolution of the Fe ions continuously by uniform and pitting corrosion.

$$Fe + Cl^- \rightarrow Fe(Cl^-) \tag{11}$$

$$Fe(OH) + Fe(Cl^-) \rightarrow Fe + FeOH^+ + Cl^- + 2e \tag{12}$$

$$FeOH^+ + H^+ \rightarrow Fe^{2+} + H_2O \tag{13}$$

$$Fe + 2Cl \rightarrow FeCl_2 + 2e^- \tag{14}$$

$$FeCl_2 + Cl^- \rightarrow FeCl_3 + e^- \tag{15}$$
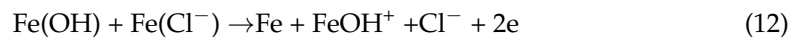
The ferrous chloride formed on the steel surface shown in equation (14) cannot stay longer on the surface and gets converted into an interface before getting dissolved in the solution by leaving the surface. The chloride ions present in the solution further react with the formed ferrous chloride on the surface as well as the dissolved ion in the solution to form ferric chloride, which is given in Equation (15) [45]. The formed ferric chloride ($FeCl_3$) is another corrosion product leading to the formation of bead-like spots on the surface of the metal [46]. These iron chloride compounds further initiate the dissolution of iron ions themselves by attacking the surface of the metal either after the chloride compounds dissolve in to the solution or beneath the formed corrosion product, which leads to the formation of pits [45]. The corrosion products formed by the reactions of various ions in the presence of NaCl, different flow condition, and applied permanent magnetic field contribute in changing the I_{corr}, E_{Corr}, β_a, β_c values by which the corrosion rate changes, which can be observed in Table 2.

4.1. Effect of Magnetic Field on the Corrosion Mechanism of API 5L X65

The magnetic properties of a material depend on different factors, such as microstructure, chemical composition, heat treatment, and mechanical conditions [47]. The study conducted by Erwing in 1893 shows that the non-magnetic inclusion, mainly carbide, plays an important role in the metal magnetic properties [48]. Iron derivatives, such as carbon steel and stainless steel, are differentiated based on the presence of these non-magnetic inclusions. In this case from Table 1, it is understood that the amount of carbon is only 0.11 and, hence, shows very high magnetic properties. Metals exhibiting very good magnetic properties are categorized as ferromagnetic materials. Ferromagnetic materials possess a permanent magnetic moment in the absence of an external magnetic field, which helps to attain very high magnetization. Unlike other materials, ferromagnetic materials have their magnetic moment aligned in the same direction, which results in an uncancelled magnetic moment among themselves. For ferromagnetic material, the magnetic dipole moments, which are the electrically charged particles in a material, orient themselves in the same direction in a particular domain, as shown in Figure 7. Domains are the regions where the magnetic dipole moments arrange themselves in the same direction within the domain wall. When a magnetic field is applied, the magnetic dipoles present in different domains orient in the same direction that is favorable to the applied magnetic field.
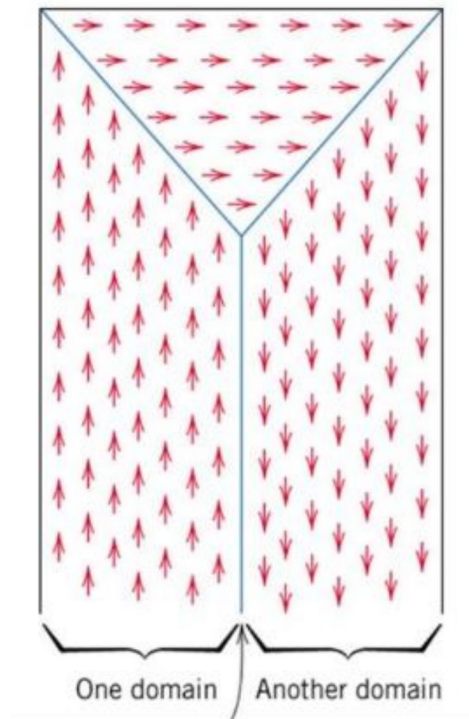
Figure 7. Schematic depiction of domains in a ferromagnetic material [49].

When a magnetic field is applied to a ferromagnetic material in the presence of an aqueous medium, the electrochemical behavior of these materials is driven by a magnetohydrodynamic mechanism. Consistent with a magnetohydrodynamic mechanism, when a magnetic field is applied to an electrochemical reaction, two kinds of body forces are introduced to the system: the Lorentz force and the magnetic field gradient force (MFGF). The MFGF comes into existence when an external magnetic field is imposed on a ferromagnetic material, which results in the deviation of magnetic flux lines. This force drives the paramagnetic particles to high magnetic flux density areas, causing a gradient concentration of paramagnetic ions, and acts on the regions where the magnetic field gradient exists [34,50]. The magnetic field force, $\vec{F}_{\nabla B}$ is given in Equation (16) where χ_m is molar susceptibility, B the magnetic flux density, c the concentration, $\vec{\nabla}B$ the gradient magnetic flux density, and μ_o. the magnetic permeability of vacuum.

$$\vec{F}_{\nabla B} = \frac{\chi_m c B \vec{\nabla}B}{\mu_o} \tag{16}$$

Lorentz force originates when there is movement of particles caused by the combined effect of the electric current and magnetic field. Lorentz force $\vec{F}_L$. is given in Equation (17) where $\vec{J}$. is the current density and $\vec{B}$ is the magnetic flux density.

$$\vec{F}_L = \vec{J} \times \vec{B} \tag{17}$$

Lorentz force is maximal when the $\vec{J}$ is perpendicular to $\vec{B}$ and zero when $\vec{J}$. is parallel to $\vec{B}$. From Table 2 and Figure 8, it can be observed that the magnetic field increases the corrosion rate of the API 5L X65 samples. At 0 m/s, the corrosion rate for the no magnetic field condition is measured as 0.28 mmpy. As soon as a magnetic field of a N–S orientation is applied over the material, the corrosion rate increased by approximately 20%, resulting in 0.33 mmpy, and, when a N–N magnetic field is applied, the corrosion

rate increased by more than 250%, resulting in 1.00 mmpy. As the velocity increases to 1 m/s, the corrosion rate is measured as 0.70 mmpy for a no magnetic field condition. Again, as mentioned above, when a N–S magnetic field is applied, the corrosion rate is increased to 1.11 mmpy, which is almost 60% more than the no magnetic field condition, and, when a N–N magnetic field is applied, the corrosion rate increased to 1.54 mmpy, which is 120% higher than the no magnetic field condition. The corrosion process due to a magnetic field does not change when a flow is introduced to the system. It only aggravates the corrosion process, causing more corrosion by the dissolution of ions on the surface. Similar to what is observed at 1 m/s, the corrosion rate is higher at 2 m/s with 0.78 mmpy in the no magnetic field condition, 1.47 mmpy for the N–S magnetic field, which is almost 50% higher than the no magnetic field condition, and 2.39 mmpy for the N–N magnetic field, which is 200% higher than the no magnetic field condition. Hence, it is clear that the presence of a magnetic field increases the corrosion rate of the samples irrespective of any kind of environment.
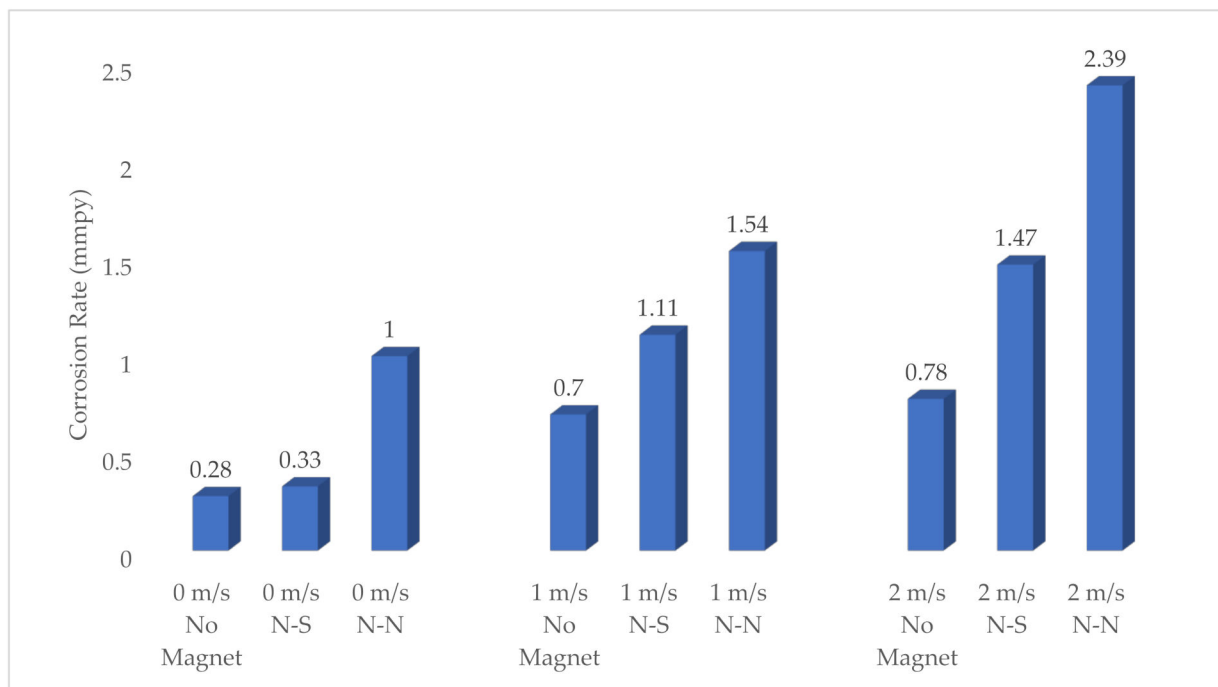
Figure 8. Corrosion rate of API 5L X65 samples at different magnetic field and different flow velocities.

As discussed above, the magnetohydrodynamic mechanism plays an important role in increasing the corrosion rate. However, in this case, as there is no impressed current in the corrosion process, the Lorentz force is weak and can be neglected [50]. Hence, the complete corrosion process is caused by the MFGF. The MFGF presence in the electrochemical system, when an external magnetic field is applied, causes the movement of anions and cations. For a ferromagnetic material such as API 5L X 65, the dissolution of ions by the anodic reaction results in the formation of paramagnetic ions. By applying a magnetic field to these paramagnetic ions, the MFGF causes the concentration of paramagnetic ions on the surface of the metal [21,34,51]. The MFGF, which has the same direction as the movement of paramagnetic ions, results in the dissolution of the protective film on the surface, and, consequently, the surface corrosion increases. This phenomenon of the breakage of the protective layer can be observed from Nyquist plots in Figure 5 and Table 3. For zero velocity, the R_f value at A1 is observed as 490.3 Ωcm^2, which then reduces to 373.8 Ωcm^2 as soon as a a N–S magnetic field is applied. It again reduces to 100.3 Ωcm^2 when a N–N magnetic field is applied, depicting that the MFGF causes the dissolution of the protective layer. The reason that the N–N magnetic field condition results in the highest corrosion

rate out of all the cases is that, for a N–N condition, there is no cancellation of the magnetic fluxes by which aggravation will occur from both of the directions, causing concentration of ions from both the sides. However, in the case of N–S condition, there is a cancellation of the magnetic fluxes between the two different magnets, causing decreased concentration of ions on the surface.

4.2. Effect of Flow Velocity on the Corrosion Mechanism of API 5L X65

The corrosion rate for the API 5L X65 has been observed to be higher for the dynamic condition than the static condition from the potentiodynamic polarization data and the EIS data. It is obvious that the mass transfer rate increases under the dynamic condition because the fluid flow causes shear stress on the sample surface, leading to the hindering of the protective oxide layer formation [6,52]. This is observed from the EIS data given in Table 3, where the R_f values are very high for the static condition and very low for the dynamic condition. The Nyquist plots under condition A1, given in Figure 5a, show the largest diameter capacitance semicircle obtained: an R_{ct} value of 3310 Ωcm^2 and an R_f value of 490.3 Ωcm^2. As soon as flow is induced in the system, the diameter of the capacitance semicircle decreases, as shown in Figure 5b,c, giving an R_{ct} value of 1420 Ωcm^2 and an R_f value of 4.295 Ωcm^2 for condition B1, and an R_{ct} value of 723.9 Ωcm^2 and an R_f value of 4.778 Ωcm^2 for condition C1.

Depending upon oxygenated and deoxygenated systems, the corrosion behavior of metals and alloys can change, which makes predicting the effect of hydrodynamics on corrosion rates and the corrosion mechanism difficult. The effect of flow velocities on the corrosion rate with a magnetic field and without a magnetic field is shown in Figure 9. In this oxygenated flow system, the corrosion rates tend to increase with flow velocities in all the conditions studied. When there is no magnetic field present, the corrosion rate is 0.28 mmpy at zero velocity, and, when the flow velocity is increased to 1 m/s (Reynolds Number ≈ 19,000), the corrosion rate increases to 0.70 mmpy, which is one and a half times higher than zero flow. At 2 m/s (Reynolds Number ≈ 38,000), the corrosion rate reaches 0.78 mmpy, showing an 11% increase as compared to a velocity of 1m/s and two times higher as compared to zero flow. When a magnetic field is introduced, similar trends are observed with an increase in flow velocity. In the N-S magnetic orientation, at zero flow, the corrosion rate is 0.33 mmpy, and a 230% to 350% increase can be observed for flow velocities of 1 m/s and 2 m/s, respectively. Similarly, for the N-N magnetic orientation, at zero flow, the corrosion rate is 1.00 mmpy, and a 53% to 140% increase can be observed for flow velocities of 1 m/s and 2 m/s, respectively. When the flow velocity is increased, the hydrodynamic force removes the corrosion products formed, but it can increase the dissolved oxygen diffusion to the material surface. This combined effect alters the corrosion rates with flow. The EDX data from Table 7 show that, as the flow rate increases, the elemental concentration of the oxygen rate on the surface for A3, B3, and C3 conditions increases, as expected. However, the action of hydrodynamic forces to reduce corrosion product deposits on the metal surface at higher fluid velocities could not be observed. The authors believe that this may be due to the magnetic field applied to the material, which resists the removal of the corrosion product from the metal surface. From the SEM and surface roughness images given in Tables 4 and 7, we can see that, at zero velocity, we observe predominantly uniform corrosion across the material, and, at higher velocities of 1 m/s and 2 m/s, oxygen concentration cells are formed on the surface, resulting in localized corrosion, causing small pits.
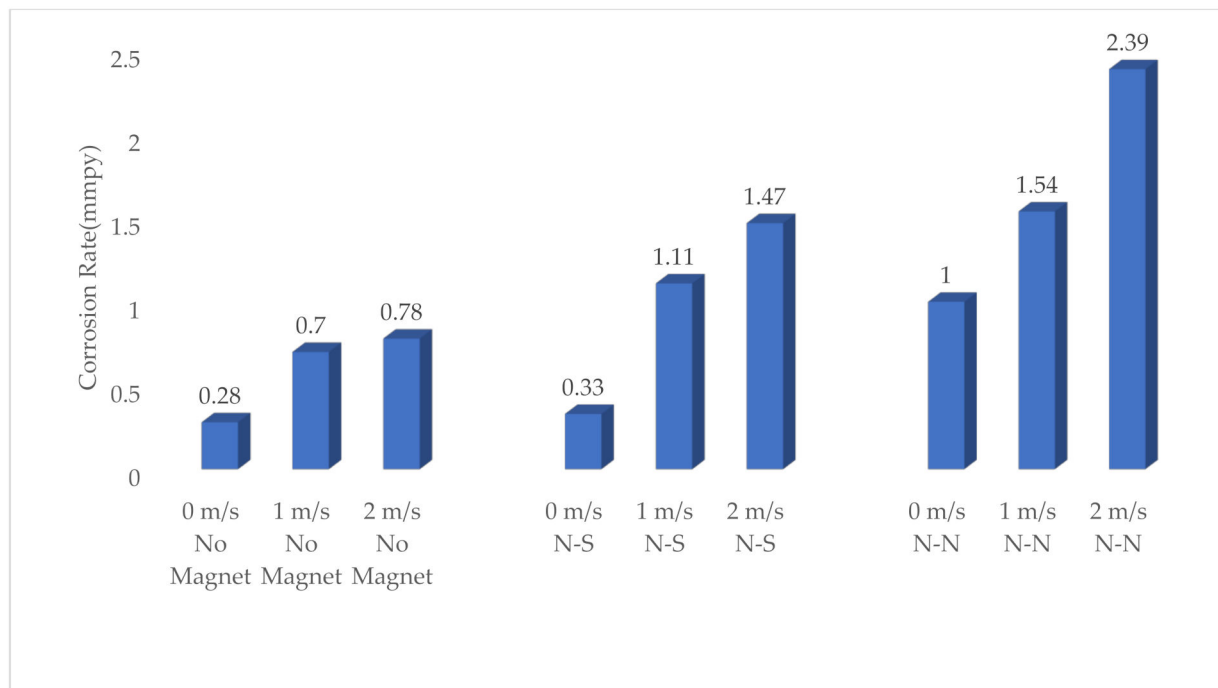
Figure 9. Corrosion rate of API 5L X65 samples at different flow velocities.

5. Conclusions

The effect of a magnetic field and fluid velocity on API 5L X65 carbon steel material in an aqueous NaCl solution was studied with the help of a polarization technique, EIS, and microscopic observation. For the static condition, the presence of a 0.15 T magnetic field applied to the sample surface aggravated the corrosion process by the concentration of paramagnetic ions at the maximum magnetic flux density regions. When compared to a no magnetic field condition, the corrosion rate was almost four times higher, and the surface showed more of a uniform corrosion. In the absence of a magnetic field, when a flow was induced to the system, the corrosion rate increased, obviously due to the increase in the dissolved oxygen supplied to the surface of the material. By this dissolution, the formation of an oxide protective layer slowed when compared to the static condition. The surface showed more localized corrosion, causing pits as the fluid velocity was increased. For both a magnetic field and flow-induced system, the corrosion rate was relatively very high as it involves the influence of both the MFGF and hydrodynamics. These two mechanisms, by their combined effect, increased the anodic dissolution of the iron, leading to an increase in the oxidation reaction, causing a higher corrosion rate than the no magnetic field, zero flow condition.

Author Contributions: Conceptualization, S.P., A.R., N.V. and O.S.; methodology, S.P. and A.R.; software, S.P.; validation, S.P.; investigation, S.P.; resources, N.V.; writing—original draft preparation, S.P.; writing—review and editing, N.V. and O.S.; visualization, S.P.; supervision, N.V.; All authors have read and agreed to the published version of the manuscript.

Institutional Review Board Statement: Not applicable.

Informed Consent Statement: Not applicable.

Data Availability Statement: The data presented in this study are available on request from the corresponding author.

Conflicts of Interest: The authors declare no conflict of interest.

References

1. Biezma, M.; Andrés, M.; Agudo, D.; Briz, E. Most fatal oil & gas pipeline accidents through history: A lessons learned approach. *Eng. Fail. Anal.* **2020**, *110*, 104446. [CrossRef]
2. Alawadhi, K.; Aloraier, A.S.; Joshi, S.; Alsarraf, J.; Swilem, S. Investigation on Preferential Corrosion of Welded Carbon Steel Under Flowing Conditions by EIS. *J. Mater. Eng. Perform.* **2013**, *22*, 2403–2410. [CrossRef]
3. Vanaei, H.; Eslami, A.; Egbewande, A.J. A review on pipeline corrosion, in-line inspection (ILI), and corrosion growth rate models. *Int. J. Press. Vessel. Pip.* **2017**, *149*, 43–54. [CrossRef]
4. Khaliq, A. Analysis of steel pipeline corrosion in the context of oil and gas industry. *Sci. Int.* **2021**, *33*, 29–32.
5. Wang, B.; Wang, Y.; Li, Q.; Li, H.; Zhang, L.; Lu, M. Effect of chromium on the corrosion behavior of low Cr-bearing alloy steel under an extremely high flow rate. *RSC Adv.* **2020**, *10*, 35302–35309. [CrossRef]
6. Zhang, G.; Zeng, Y.; Guo, X.; Jiang, F.; Shi, D.; Chen, Z.J. Electrochemical corrosion behavior of carbon steel under dynamic high pressure H_2S/CO_2 environment. *Corros. Sci.* **2012**, *65*, 37–47. [CrossRef]
7. Utanohara, Y.; Murase, M. Influence of flow velocity and temperature on flow accelerated corrosion rate at an elbow pipe. *Nucl. Eng. Des.* **2019**, *342*, 20–28. [CrossRef]
8. Liu, A.Q.; Bian, C.; Wang, Z.M.; Han, X.; Zhang, J.J. Flow dependence of steel corrosion in supercritical CO2 environments with different water concentrations. *Corros. Sci.* **2018**, *134*, 149–161. [CrossRef]
9. Liu, J.; BaKeDaShi, W.; Li, Z.; Xu, Y.; Ji, W.; Zhang, C.; Cui, G.; Zhang, R.J. Effect of flow velocity on erosion–corrosion of 90-degree horizontal elbow. *Wear* **2017**, *376*, 516–525. [CrossRef]
10. Zhang, G.; Zeng, L.; Huang, H.; Guo, X. A study of flow accelerated corrosion at elbow of carbon steel pipeline by array electrode and computational fluid dynamics simulation. *Corros. Sci.* **2013**, *77*, 334–341. [CrossRef]
11. Zhang, N.; Zeng, D.; Zhang, Z.; Zhao, W.; Yao, G. Effect of flow velocity on pipeline steel corrosion behaviour in H2S/CO2environment with sulphur deposition. *Corros. Eng. Sci. Technol.* **2018**, *53*, 370–377. [CrossRef]
12. Ajmal, T.; Arya, S.B.; Udupa, K.R. Effect of hydrodynamics on the flow accelerated corrosion (FAC) and electrochemical impedance behavior of line pipe steel for petroleum industry. *Int. J. Press. Vessel. Pip.* **2019**, *174*, 42–53. [CrossRef]
13. Xu, L.; Cheng, Y. Effect of fluid hydrodynamics on flow-assisted corrosion of aluminum alloy in ethylene glycol–water solution studied by a microelectrode technique. *Corros. Sci.* **2009**, *51*, 2330–2335. [CrossRef]
14. Rachmawati, I.D.; Nurdin, I.; Widiatmoko, P.; Devianto, H.; Irmayanti, F.; Saptohadi, S. *The Effect of Flow Rate and NaCl Concentration on the Corrosion Behavior of Carbon Steel in NaCl Solutions Containing H_2S*; IOP Conference Series; Materials Science and Engineering 778: Bristol, UK, 2020. [CrossRef]
15. Balogun, A.-L.; Matori, A.-N.; Hamid-Mosaku, I.A. A fuzzy multi-criteria decision support system for evaluating subsea oil pipeline routing criteria in East Malaysia. *Environ. Earth Sci.* **2015**, *74*, 4875–4884. [CrossRef]
16. Hossam-Eldin, A.A.; Mokhtar, W. *Electromagnetic Interference between Electrical Power Lines and Neighboring Pipelines*; IEEE: Piscataway, NJ, USA, 2008; pp. 97–102.
17. Sawma, E.; Zeitoun, B.; Harmouche, N.; Georges, S.; Hamad, M.; Slaoui, F. *Electromagnetic Induction in Pipelines due to Overhead High Voltage Power Lines*; IEEE: Piscataway, NJ, USA, 2010; pp. 1–6.
18. Li, Y.; Dawalibi, F.P. Effects of Current Unbalance and Transmission Line Configuration on the Interference Levels Induced on Nearby Pipelines. In Proceedings of the CORROSION 2004, New Orleans, LA, USA, 28 March –1 April 2004.
19. Gouda, O.E.; EL Dein, A.Z.; El-Gabalawy, M.A. Effect of electromagnetic field of overhead transmission lines on the metallic gas pipelines. *Electr. Power Syst. Res.* **2013**, *103*, 129–136. [CrossRef]
20. Ouadah, M.; Touhami, O.; Ibtiouen, R.; Benlamnouar, M.; Zergoug, M. Corrosive effects of the electromagnetic induction caused by the high voltage power lines on buried X70 steel pipelines. *Int. J. Electr. Power Energy Syst.* **2017**, *91*, 34–41. [CrossRef]
21. Hu, J.; Dong, C.; Li, X.; Xiao, K. Effects of Applied Magnetic Field on Corrosion of Beryllium Copper in NaCl Solution. *J. Mater. Sci. Technol.* **2010**, *26*, 355–361. [CrossRef]
22. Chiba, A.; Ogawa, T.J. Effects of magnetic field direaction on the dissolution of copper, zinc, and brass in nitric acid. *Corros. Eng.* **1988**, *37*, 531.
23. Lu, Z.; Yang, W. In situ monitoring the effects of a magnetic field on the open-circuit corrosion states of iron in acidic and neutral solutions. *Corros. Sci.* **2008**, *50*, 510–522. [CrossRef]
24. Sueptitz, R.; Tschulik, K.; Uhlemann, M.; Schultz, L.; Gebert, A. Effect of high gradient magnetic fields on the anodic behaviour and localized corrosion of iron in sulphuric acid solutions. *Corros. Sci.* **2011**, *53*, 3222–3230. [CrossRef]
25. Zheng, B.; Li, K.; Liu, H.; Gu, T. Effects of Magnetic Fields on Microbiologically Influenced Corrosion of 304 Stainless Steel. *Ind. Eng. Chem. Res.* **2014**, *53*, 48–54. [CrossRef]
26. Hinds, G.; Coey, J.M.D.; Lyons, M. Influence of magnetic forces on electrochemical mass transport. *Electrochem. Commun.* **2001**, *3*, 215–218. [CrossRef]
27. Shinohara, K.; Aogaki, R. Magnetic Field Effect on Copper Corrosion in Nitric Acid. *Electrochemistry* **1999**, *67*, 126–131. [CrossRef]
28. Aaboubi, O.; Chopart, J.-P.; Douglade, J.; Olivier, A.; Gabrielli, C.; Tribollet, B. Magnetic Field Effects on Mass Transport. *J. Electrochem. Soc.* **1990**, *137*, 1796–1804. [CrossRef]
29. Costa, I.; Oliveira, M.; De Melo, H.; Faria, R.J. The effect of the magnetic field on the corrosion behavior of Nd–Fe–B permanent magnets. *J. Magn. Magn. Mater.* **2004**, *278*, 348–358. [CrossRef]

30. Pondichery, S. A Study on the Effect of Magnetic Field on the Corrosion Behavior of Materials. Master of Science Thesis, The University of Texas, Arlington, TX, USA, December 2014.
31. Li, X.; Zhang, M.; Yuan, B.; Li, L.; Wang, C.J. Effects of the magnetic field on the corrosion dissolution of the 304 SS FeCl$_3$ system. *Electrochim. Acta* **2016**, *222*, 619–626. [CrossRef]
32. Ručinskien, A.; Bikulčius, G.; Gudavičiūt, L.; Juzeliūnas, E. Magnetic field effect on stainless steel corrosion in FeCl3 solution. *Electrochem. Commun.* **2002**, *4*, 86–91. [CrossRef]
33. Chiba, A.; Ogawa, T.J. Influence of angle of the line of magnetic force on the dissolution of copper, zinc and brass in nitric acid solution. *Corros. Eng.* **1988**, *37*, 595–600. [CrossRef]
34. Zhang, X.; Wang, Z.; Zhou, Z.; Yang, G.; Cai, X. Impact of magnetic field on corrosion performance of Al–Mg alloy with different electrode potential phases. *Intermetallics* **2021**, *129*, 107037. [CrossRef]
35. Ravikumar, A.; Rostron, P.; Vahdati, N.; Shiryayev, O. Parametric Study of the Corrosion of API-5L-X65 QT Steel Using Potentiostat Based Measurements in a Flow Loop. *Appl. Sci.* **2021**, *11*, 444. [CrossRef]
36. Almahmoud, S.; Shiryayev, O.; Vahdati, N.; Rostron, P. *Pipeline Internal Corrosion Sensor Based on Fiber Optics and Permanent Magnets*; International Society for Optics and Photonics: Bellingham, WA, USA, 2018; p. 1059836.
37. AlMahmoud, S.; Shiryayev, O.; Vahdati, N.; Rostron, P. Detection of Internal Metal Loss in Steel Pipes and Storage Tanks via Magnetic-Based Fiber Optic Sensor. *Sensors* **2018**, *18*, 815. [CrossRef]
38. Aljarah, A.; Vahdati, N.; Butt, H. Magnetic Internal Corrosion Detection Sensor for Exposed Oil Storage Tanks. *Sensors* **2021**, *21*, 2457. [CrossRef]
39. Han, J.; Carey, J.W.; Zhang, J. Effect of sodium chloride on corrosion of mild steel in CO2-saturated brines. *J. Appl. Electrochem.* **2011**, *41*, 741–749. [CrossRef]
40. May, M.J. Corrosion behavior of mild steel immersed in different concentrations of NaCl solutions. *J. Sebha Univ.* **2016**, *15*, 1–12.
41. Fontana, M.G. *Corrosion Engineering*; Tata McGraw-Hill Education: New York, NY, USA, 2005.
42. Sherif, E.-S.M.; Almajid, A.A.; Khalil, K.A.; Junaedi, H.; Latief, F.J. Electrochemical studies on the corrosion behavior of API X65 pipeline steel in chloride solutions. *Int. J. Electrochem. Sci.* **2013**, *8*, 9360–9370.
43. Sherif, E.-S.M.; Almajid, A.A. Anodic Dissolution of API X70 Pipeline Steel in Arabian Gulf Seawater after Different Exposure Intervals. *J. Chem.* **2014**, *2014*, 1–7. [CrossRef]
44. Sherif, E.-S.M.; Erasmus, R.; Comins, J.J. In situ Raman spectroscopy and electrochemical techniques for studying corrosion and corrosion inhibition of iron in sodium chloride solutions. *Electrochim. Acta* **2010**, *55*, 3657–3663. [CrossRef]
45. Sherif, E.-S.M.J. A comparative study on the electrochemical corrosion behavior of iron and X-65 steel in 4.0 wt% sodium chloride solution after different exposure intervals. *Molecules* **2014**, *19*, 9962–9974. [CrossRef]
46. Gilberg, M.R.; Seeley, N.J.J. The identity of compounds containing chloride ions in marine iron corrosion products: A critical review. *Stud. Conserv.* **1981**, *26*, 50–56.
47. Jiles, D.J. Magnetic properties and microstructure of AISI 1000 series carbon steels. *J. Phys. D Appl. Phys.* **1988**, *21*, 1186. [CrossRef]
48. Wilson, E.J.N. Magnetic Induction in Iron and other Metals. *Nature* **1893**, *47*, 460–461. [CrossRef]
49. Callister, W.D., Jr.; Rethwisch, D.G. *Callister's Materials Science and Engineering*; John Wiley & Sons: Hoboken, NJ, USA, 2020; p. 2020.
50. Zhao, S.; You, Z.; Zhang, X.; Li, J. Magnetic field effects on the corrosion and electrochemical corrosion of Fe$_{83}$Ga$_{17}$ alloy. *Mater. Charact.* **2021**, *174*, 110994. [CrossRef]
51. Zhao, S.; Bai, J.; You, Z.; Li, J. Effect of a magnetic field on stress corrosion cracking of Fe83Ga17 alloy. *Corros. Sci.* **2020**, *167*, 108539. [CrossRef]
52. Zhang, G.; Liu, D.; Li, Y.; Guo, X.J. Corrosion behaviour of N80 carbon steel in formation water under dynamic supercritical CO2 condition. *Corros. Sci.* **2017**, *120*, 107–120. [CrossRef]